Physics of Fluids

A Lagrangian theory of geostrophic adjustment for zonally invariant flows on a rotating spherical earth

Cite as: Phys. Fluids **33**, 066602 (2021); https://doi.org/10.1063/5.0054535
Submitted: 19 April 2021 . Accepted: 18 May 2021 . Published Online: 03 June 2021

Nathan Paldor, and David G. Dritschel

Physics of Fluids ARTICLE scitation.org/journal/phf

A Lagrangian theory of geostrophic adjustment for zonally invariant flows on a rotating spherical earth

Cite as: Phys. Fluids **33**, 066602 (2021); doi: 10.1063/5.0054535
Submitted: 19 April 2021 · Accepted: 18 May 2021 ·
Published Online: 3 June 2021

Nathan Paldor[1,a] and David G. Dritschel[2]

AFFILIATIONS

[1]Fredy and Nadine Herrmann Institute of Earth Sciences, Hebrew University of Jerusalem, Jerusalem 91904, Israel
[2]Mathematical Institute, University of St Andrews, St Andrews, Fife, KY16 9SS, United Kingdom

[a]Author to whom correspondence should be addressed: nathan.paldor@mail.huji.ac.il

ABSTRACT

We examine the late-time evolution of an inviscid zonally symmetric shallow-water flow on the surface of a rotating spherical earth. An arbitrary initial condition radiates inertia–gravity waves that disperse across the spherical surface. The simpler problem of a uniformly rotating (f-plane) shallow-water flow on the plane radiates these waves to infinity, leaving behind a nontrivial steady flow in geostrophic balance (in which the Coriolis acceleration balances the horizontal hydrostatic pressure gradient). This is called "geostrophic adjustment." On a sphere, the waves cannot propagate to infinity, and the flow can never become steady due to energy conservation (at least in the absence of shocks). Nonetheless, when energy is conserved a form of adjustment still takes place, in a time-averaged sense, and this flow satisfies an extended form of geostrophic balance dependent only on the conserved mass and angular momentum distributions of fluid particles, just as in the planar case. This study employs a conservative numerical scheme based on a Lagrangian form of the rotating shallow-water equations to substantiate the applicability of these general considerations on an idealized aqua-planet for an initial "dam" along the equator in a motionless ocean.

I. INTRODUCTION

Geostrophic adjustment theory describes the intricate manner in which an arbitrary initial rotating stratified flow transforms to a final, steady, and geostrophically balanced state. The paramount importance of this theory is clear in view of the dominance of geostrophic balance on scales larger than mesoscale (in the ocean) and synoptic scale (in the atmosphere).[1,2] The theory was first developed in the 1930s on the f-plane[3,4] and since then, several follow-up studies[5–8] have extended the original results to various initial conditions, including the classical fluid dynamical problem of a dam break in a fluid initially at rest.[7]

Accounting for latitudinal variations in the Coriolis frequency (or background planetary vorticity), even in planar geometry through the β effect, greatly complicates the analysis and is the reason for the slow progress in advancing the geostrophic adjustment theory beyond the f-plane. In this study, we employ a Lagrangian formulation of the dynamics to study the adjustment process on a rotating spherical planet. We consider the simplest relevant model, namely, the one-dimensional, zonally symmetric shallow-water model that ignores longitudinal variations of both velocity and height. This approximation limits the applicability of the model to zonal flows.

As in all geostrophic adjustment theories, the analysis involves a derivation of the final, presumably steady, geostrophic or "balanced" state together with a description of the transient waves that transform the initial state to the final state. Since the surface of a sphere is a bounded domain, the transient waves cannot propagate to infinity and hence, in contrast to the classical studies mentioned above, the integral (over the entire sphere) of the initial state's energy must be conserved. The conserved energy must, therefore, be divided between the steady balanced state and the transient waves. As the energy in the balanced state is fixed, then so must be the energy in the waves. Thus, because the domain is bounded, the waves cannot escape (as in an unbounded plane), and in the absence of dissipation they may mask the underlying steady balanced flow for all time.

The Lagrangian approach adopted here is necessary to isolate the underlying steady balanced state having the same invariants as the initial state. That is, each fluid "particle" (here a latitude circle) in the

balanced state must have the same mass and angular momentum as that in the initial state. This novel Lagrangian formulation allows one to derive the appropriate nonlinear balance equation (in a Lagrangian coordinate) determining the balanced state corresponding to any prescribed initial state. The Lagrangian formulation is also useful numerically for studying the transient flow evolution, as conservation of mass, angular momentum, and potential vorticity on each fluid particle can be exactly satisfied at all times. The Lagrangian approach is unique in that no high-order viscous terms are required to stabilize the numerical solution. This is of primary importance when studying the nonlinear rotating shallow-water equations in spherical coordinates that struggle with the coordinate singularity at the poles.[9,10]

In more complex two-dimensional and layerwise-two-dimensional flows, an (at least partially) Lagrangian formulation has proved highly beneficial in the study of fundamental aspects of geophysical fluid dynamics. The suite of "contour advection" methods[11–15] enforces material conservation of potential vorticity by tracking material contours in a Lagrangian manner, but otherwise use Eulerian (fixed-grid) methods for efficiency. These methods originate in the fully Lagrangian "contour dynamics" method,[16–18] first applied to two-dimensional flows in an unbounded domain. Contour dynamics requires an invertable linear relation between (potential) vorticity and the flow field (e.g., through a Green function). Contour advection relaxes this requirement by making use of Eulerian inversion methods, allowing access to a much wider range of fluid models. The Lagrangian formulation has been extensively employed in studies of inertial (particle) motion on a rotating sphere and the rotating spherical earth.[19,20]

A comment is in order regarding our use of the term "spherical earth" in the title instead of "sphere." On a sphere that rotates at the Earth's rotation frequency, the centrifugal acceleration exceeds the Coriolis acceleration even for speeds of 100 ms^{-1}. However, the equatorial bulge that results from the slight eccentricity of the shape of the Earth's surface ($\sim$0.003) adds a poleward directed component of the gravitational acceleration that balances the equatorward directed centrifugal acceleration. Since the Earth's eccentricity is small, and since its effect on wave dynamics is second order,[21] the fractional error expected from the approximation of Earth's ellipsoidal surface by a sphere, while ignoring the centrifugal acceleration, is only $O(10^{-5})$. Here, we consider this negligible.

Another important point is that we are not directly considering the problem of "balance," a hypothetical state (for a general two-dimensional flow) in which inertia–gravity waves are absent.[22–26] Such a state is often constructed by "PV inversion," using the definition of potential vorticity alongside a pair of "balance relations" that effectively filter the inertia–gravity waves. In this study, the zonal symmetry means that there is an exact balanced state, a completely stationary state, entirely determined by the Lagrangian mass and angular momentum distributions. These distributions determine the potential vorticity distribution for zonal flows. The focus of this study is instead on the time-dependent problem, specifically the role played by inertia–gravity waves generated from the initial conditions while the slowly propagating Rossby waves are eliminated by the assumed zonal symmetry. Notably, all unsteadiness in zonal flows may be attributed to inertia–gravity waves, the imbalanced motions. Our objective is to examine how such flows adjust to the underlying steady balanced state, at least in a time-averaged sense.

This paper is organized as follows. In Sec. II, the Lagrangian forms of the zonally symmetric spherical shallow-water equations are derived. From these, a single second-order nonlinear ordinary differential equation (ODE) is obtained for the balanced flow consistent with the initial state's distributions of mass and angular momentum—this appears to be new. The eigenvalue problem for the unsteady linear waves is also discussed, together with the numerical methods employed. The unsteady flow dynamics is described in detail in Sec. III for a specific but representative case. Here, it is shown that the time-averaged flow is nearly identical to the balanced flow, obtained independently. Balance is then the focus of Sec. IV, which explores the wider parameter space and discusses various flow properties. Our conclusions are offered in Sec. V.

II. FORMULATION OF THE LAGRANGIAN MODEL AND ITS NUMERICAL METHOD OF SOLUTION

The shallow-water equations possess a number of fundamental conservation properties due to underlying symmetries. Besides mass, angular momentum, and total energy (kinetic plus potential), potential vorticity (circulation) is locally conserved; that is, it remains constant on fluid particles (in the absence of forcing and dissipation). In a sense, mass is also locally conserved, but following infinitesimally small deformable fluid elements. For the zonally symmetric flows considered here, angular momentum also becomes locally conserved, that is, it does not change following each moving latitude.

It would therefore appear useful to cast the equations of motion in Lagrangian terms, to the extent possible (see below). In this way, conservation is built in directly (apart from energy, which is an integral invariant). This results in a pair of equations for each "particle" (really a latitude circle), one for the rate of change of its latitude and another for the rate of change of its meridional velocity. This is analogous to a particle in a force field, except here there are an infinite number of particles, and they interact locally through hydrostatic pressure variations.

A. Equations of motion

We next derive the Lagrangian forms of the zonally symmetric shallow-water equations from their standard Eulerian forms. These Lagrangian forms appear to be new and are especially useful for simulating the evolution of weakly to moderately nonlinear flows in a very nearly conservative manner. Their steady versions also enable one to link the underlying balanced state to any initial state.

To set notation, let u and v be the zonal and meridional velocity components and h be the local fluid height (here for simplicity above a flat bottom) divided by the mean fluid depth H. Let ϕ stand for latitude and t for time. Let Ω be the background rotation rate, and consider the fluid motion in a frame of reference rotating at this rate. Let g be the acceleration due to gravity and $c = \sqrt{gH}$ the short-scale gravity-wave speed. Without loss of generality, we take the radius of the planet to be 1.

The Eulerian forms of the equations read

$$\frac{\partial u}{\partial t} + v\frac{\partial u}{\partial \phi} - (u\tan\phi + f)v = 0, \tag{1}$$

$$\frac{\partial v}{\partial t} + v\frac{\partial v}{\partial \phi} + (u\tan\phi + f)u = -c^2\frac{\partial h}{\partial \phi}, \tag{2}$$

$$\frac{\partial h}{\partial t}+\frac{1}{\cos\phi}\frac{\partial(hv\cos\phi)}{\partial\phi}=0, \tag{3}$$

where $f=2\Omega\sin\phi$ is the Coriolis frequency (or planetary vorticity). It is convenient in what follows to define $r=\cos\phi$ as the radial distance from the z-axis (connecting the two poles), and $z=\sin\phi$. We also use $\dot{\xi}=\partial\xi/\partial t+v\partial\xi/\partial\phi$ to denote the material derivative or Lagrangian rate of change of any quantity ξ.

Equation (1) expresses conservation of angular momentum. Multiplying it by r and using $\dot{\phi}=v$, we find

$$r\dot{u}-(u+2\Omega r)z\dot{\phi}=0, \tag{4}$$

which shows that angular momentum $U=r(u+\Omega r)$ is materially conserved: $\dot{U}=0$. This motivates introducing a Lagrangian label a for each fluid particle, and denoting the latitude of the particle by $\phi(a,t)$. The label itself could be the initial latitude, in which case $\phi(a,0)=a$. Material conservation of angular momentum is then equivalent to the statement that U depends only on a.

Equation (3) expresses conservation of mass: the mass $\mathrm{d}M$ between any two material latitudes $\phi(a,t)$ and $\phi(a+\mathrm{d}a,t)$ is fixed for all time. As differential area on a spherical surface is proportional to $r\mathrm{d}\phi$, it follows that $\mathrm{d}M\equiv hr\mathrm{d}\phi$ depends only on a. That is,

$$M'(a)=h(a,t)r(a,t)\phi'(a,t) \tag{5}$$

depends only on a; here a prime denotes differentiation with respect to a, and $r(a,t)=\cos(\phi(a,t))$. Hence, given $M'(a)$, at any time the height distribution is given by

$$h(a,t)=\frac{M'(a)}{r(a,t)\phi'(a,t)}. \tag{6}$$

Similarly, the angular momentum distribution $U(a)$ determines the zonal velocity from

$$u(a,t)=\frac{U(a)}{r(a,t)}-\Omega r(a,t). \tag{7}$$

Potential vorticity conservation, $Q=Q(a)$, is a by-product of the conservation of M and U. From the definition, we have

$$Q=\frac{\zeta+f}{h}, \tag{8}$$

where ζ is the relative vorticity,

$$\zeta=-\frac{1}{r}\frac{\partial(ru)}{\partial\phi}=-f-\frac{U'}{r\phi'}, \tag{9}$$

by (7). It follows that

$$Q=-\frac{U'}{hr\phi'}=-\frac{U'}{M'} \tag{10}$$

by (5). This proves that Q is a function of a only, i.e., Q is materially conserved.

The remaining Eq. (2) of the shallow-water set for the meridional velocity v, together with $v=\dot{\phi}$, provide the dynamical evolution equations in the Lagrangian formulation. Using (7) to replace u in (2), these equations are

$$\dot{\phi}=v, \tag{11}$$

$$\dot{v}=\frac{z}{r}\left(\Omega^2r^2-\frac{U^2}{r^2}\right)-c^2\frac{\partial h}{\partial\phi}. \tag{12}$$

(The reader is reminded that $r=\cos\phi$ and $z=\sin\phi$.) Only the hydrostatic acceleration $-c^2\partial h/\partial\phi$ is left in the Eulerian form. It can be converted using (6) for h and the chain rule $\partial h/\partial\phi=(1/\phi')\partial h/\partial a$. This is a nonlocal term since it depends on ϕ' and ϕ''. It is through this term that all particles interact with one another.

The boundary conditions are that $\phi=\pm\pi/2$ at the north and south poles, and $v=0$ there for consistency. Typically, the angular momentum $U\sim r^2$ near each pole, so v remains zero at each pole only if $\partial h/\partial\phi=0$ there.

Equations (11) and (12) conserve total energy (the Hamiltonian, an integral invariant), the sum of kinetic and (available) potential energy

$$\mathcal{H}=\frac{1}{2}\int_{-\pi/2}^{\pi/2}\big(u(a,t)^2+v(a,t)^2+c^2(h(a,t)-1)\big)M'(a)\,\mathrm{d}a. \tag{13}$$

This is actually the total energy divided by the mean depth H due to the scaling adopted for h.

Numerically, Eqs. (11) and (12) are simple to solve as the only coupling term is the hydrostatic acceleration. We discretize the system into $n+1$ particles (latitudes ϕ_j), indexed $j=0,1,\ldots,n$, equally spaced in the label a (reserving $j=0$ and n for the fixed polar values, $\phi_0=-\pi/2$ and $\phi_n=\pi/2$). From a prescribed initial height distribution $h(\phi,0)$, we calculate the fixed mass $m_j=\Delta M_j$ between adjacent latitudes ϕ_j by integrating (5) at $t=0$

$$m_j=\int_{\phi_{j-1}}^{\phi_j}h(\phi,t=0)\cos\phi\,\mathrm{d}\phi. \tag{14}$$

This is also required to hold for all subsequent times $t>0$. Between latitudes $\phi_j(t)$ and $\phi_{j+1}(t)$ for $j=0,1,\ldots,n-1$, the height h is represented by the quadratic spline

$$h=h_j+\alpha_jp+\beta_jp^2\quad\text{with}\quad p\equiv\frac{\phi-\phi_j}{\phi_{j+1}-\phi_j}, \tag{15}$$

with the coefficients h_j, α_j, and β_j determined by: (a) enforcing continuity of h and $\partial h/\partial\phi$ at each internal latitude ϕ_j ($j=1,2,\ldots,n-1$), (b) requiring (14) to hold in each interval ($j=1,2,\ldots,n$), and (c) requiring $\partial h/\partial\phi=0$ at each pole. This gives $3n$ conditions to determine the $3n$ coefficients h_j, α_j, and β_j ($j=0,1,\ldots,n-1$). Note $h_n=h_{n-1}+\alpha_{n-1}+\beta_{n-1}$. The resulting system can be put into a simple tri-diagonal form (see the Appendix) and is readily solved in $O(n)$ operations. This provides $\partial h/\partial\phi$ at each ϕ_j, needed to calculate $\dot{v}_j$ in (12).

Besides the mass distribution, the initial meridional velocity $v(a,0)$ and angular momentum distribution $U(a)$ must be specified. The latter is calculated from the initial zonal velocity field $u(\phi,0)$, taking $\phi(a,0)=a$ for simplicity. Then $U(a)=r(a,0)(u(a,0)+\Omega r(a,0))$ with $r(a,0)=\cos(\phi(a,0))=\cos a$. The time integration is carried out using a fourth-order Runge–Kutta method, with a time step Δt taken sufficiently small to resolve the fastest gravity waves (ensuring numerical stability and excellent energy conservation).

B. Steady flow: Balance

The theory of geostrophic adjustment argues that any initial state will tend to a steady balanced flow having the same invariants $M(a)$

and $U(a)$ as $t \to \infty$. While this scenario is strictly prohibited on a bounded surface like a sphere, due to energy conservation, we will see below that the steady balanced flow is often (if not always) found upon time averaging over a sufficiently long period T. Indeed, if we time average (11), the LHS is bounded by π/T, and letting $T \to \infty$ shows that the time-averaged meridional velocity v must be zero for all particles a in this limit. If we time average (12), however, we must assume that $v(a, t)$ remains bounded pointwise to conclude that the LHS vanishes as $T \to \infty$. We cannot guarantee this using energy conservation, but it is plausible.

It is therefore of interest to compute the steady solutions of (11) and (12), for specified angular momentum and mass distributions $U(a)$ and $M(a)$. Then $v = 0$, and using (6) to substitute for $h(a)$ in (12), we obtain the nonlinear balance equation

$$\frac{c^2}{\phi'}\frac{\mathrm{d}}{\mathrm{d}a}\left(\frac{M'}{r\phi'}\right) = \frac{z}{r}\left(\Omega^2 r^2 - \frac{U^2}{r^2}\right), \tag{16}$$

where $r = \cos(\phi(a))$ and $z = \sin(\phi(a))$. This is a second-order nonlinear boundary value problem for $\phi(a)$, with Dirichlet boundary conditions $\phi(\pm\pi/2) = \pm\pi/2$. Notably, all steady zonal flows on a spherical earth satisfy (16). Once a solution $\phi(a)$ is obtained, the balanced height and zonal velocity distributions are found from (6) and (7), i.e.,

$$h = \frac{M'}{r\phi'} \quad \text{and} \quad u = \frac{U}{r} - \Omega r. \tag{17}$$

One can also calculate the relative vorticity ζ from (9).

For $M = \sin a$ and $U = \Omega\cos^2 a$, (16) admits the solution $\phi = a$. This corresponds to a flow at rest $u = 0$ having a uniform height $h = 1$. Otherwise, (16) is a highly nonlinear equation, and we must resort to a numerical solution. Here, (16) is solved on an equally spaced grid in a. Starting with an initial guess $\phi(a) = a$, subsequent guesses are obtained by linearizing (16) about the previous guess, approximating ϕ' and ϕ'' by centered differences, and solving the resulting tri-diagonal problem for the perturbation $\Delta\phi$. Under-relaxation is used by adding only half of $\Delta\phi$ to the previous guess ϕ to form the new guess (this is essential for convergence). When $\max|\Delta\phi| < 10^{-12}$, we accept $\phi(a)$ as the solution. Notably, this method even works under extreme conditions in which the fluid depth h nearly vanishes (incipient out-cropping).

C. Linear waves

Besides steady motions, Eqs. (11) and (12) admit propagating inertia–gravity waves, which cause particle oscillations (latitudinal displacements) and which fundamentally depend on both rotation and stratification (gravitational restoration of the free surface). A general initial condition can be thought of as a collection of these waves and an underlying steady balanced flow. Here we focus on the linear problem and consider only a basic state at rest. We shall see that the results are nonetheless relevant to the nonlinear problem.

A basic state at rest ($u = v = 0$, $h = 1$) corresponds to the mass and angular momentum distributions $M = \sin a$ and $U = \Omega\cos^2 a$. Both the displacement $\delta(a, t) = \phi(a, t) - a$ and the meridional velocity $v(a, t)$ are assumed to be sufficiently small to be able to linearize (11) and (12). Taking $\delta(a, t) = \hat{\delta}(a)e^{-i\omega t}$ and $v(a, t) = \hat{v}(a)e^{-i\omega t}$, where ω is the frequency, (11) and (12) are readily combined into a single linear boundary value problem for $\hat{\delta}(a)$

$$\frac{1}{r}\frac{\mathrm{d}}{\mathrm{d}a}\left(r\frac{\mathrm{d}\hat{\delta}}{\mathrm{d}a}\right) - \left(\frac{1}{r^2} + \frac{f^2}{c^2} - \frac{\omega^2}{c^2}\right)\hat{\delta} = 0, \tag{18}$$

with Dirichlet boundary conditions, $\hat{\delta}(\pm\pi/2) = 0$. Above, $r = \cos a$ and $f = 2\Omega\sin a$. This is a Sturm–Liouville problem with $\lambda = \omega^2/c^2$ serving as the eigenvalue. In general, there are an infinite number of solutions, with $0 < \lambda_1 < \lambda_2 < \ldots$ all real. Moreover, the λ_k depend only on the dimensionless parameter $L_d = c/(2\Omega)$, equal to the "Rossby deformation length" divided by the radius of the planet (here unity). Note the scaled frequency $\omega/(2\Omega) = (\omega/c)L_d$.

Figure 1 shows how $\omega/(2\Omega)$ depends on L_d for the first 10 modes ($k = 1$–10). For $L_d \gg 1$, $\omega/(2\Omega) \to \sqrt{k(k+1)}L_d$ and the corresponding eigenmodes $\hat{\delta}(a)$ are associated Legendre polynomials $P_k^1(\sin a)$. In fact, this is a good approximation until $kL_d < 1$. For small L_d, the eigenmodes approach parabolic cylinder functions which are localized within a distance of $O(L_d)$ of the equator, while $\omega/(2\Omega) \to \sqrt{(2k-1)L_d}$ as $L_d \to 0$. These dispersion curves accurately reproduce those shown in Fig. 1 of Longuet-Higgins,[27] which were derived in an Eulerian formulation using standard methods. The excellent match between the results obtained by the two vastly different methods of solution attests to the applicability and accuracy of the Lagrangian formulation of the zonally symmetric rotating shallow-water equations. These results also agree with the explicit expression derived for these waves in the limit of large L_d in Ref. 28.

III. DYNAMICS: THE DAM BREAK PROBLEM

We next examine the evolution of a flow initially at rest but with a difference in height h between the northern and southern hemisphere. Specifically, we consider the initial condition $\phi(a, 0) = a$, $v(a, 0) = 0$ and

$$h(a, 0) = 1 - A\tanh(z/w), \tag{19}$$

where $z = \sin a$, w is the width of the step, and A is an amplitude parameter. Without loss of generality, it is sufficient to consider $A > 0$. Furthermore $A < 1$ is necessary or else the fluid would outcrop at some latitude. The corresponding mass distribution $M(a) = z - Aw\log(\cosh(z/w))$. The angular momentum distribution is $U(a) = \Omega r^2$ with $r = \cos a$. In what follows, we take $\Omega = 2\pi$ without loss of generality. Then $t = 1$ corresponds to one "day."

Figure 2 depicts the flow evolution for $h - 1$, u and v (left to right) over the first day, for a dam break with $A = 0.05$, $w = 0.1$, and $L_d = 0.2$. [Here $n = 500$ intervals in a were used, but the results are closely reproducible at half and double resolution, at least up to early times ($t = 10$); thereafter solutions gradually diverge.] On the left, the initial step in $h-1$ is seen to split into two steps of nearly equal size (but opposite signs) propagating toward the poles. The one propagating toward the south pole is faster as the gravity-wave speed at the leading edge is approximately $c\sqrt{h}$ and is larger where h is larger in the southern hemisphere. This leads to an asymmetry that grows in time. It results in more nonlinear behavior in the northern hemisphere, causing small-scale ripples in $h - 1$ and v. In the zonal velocity u, jets develop on either side of the equator but then collapse (only to re-emerge repeatedly at later times). The meridional velocity is initially positive everywhere until it reverses around $t = 0.5$ then becomes

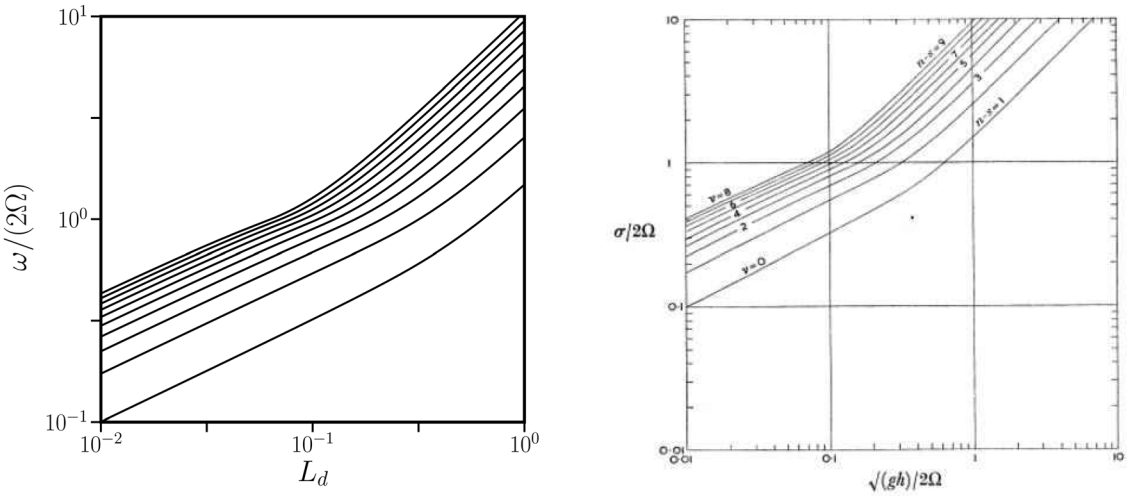

FIG. 1. Dispersion relation $\omega/(2\Omega)$ vs $L_d = c/(2\Omega)$ for inertia–gravity waves on a basic state at rest: the panel on the left shows the present results, while that on the right is Fig. 1 from Longuet-Higgins.[27] [Reproduced with permission from M. Longuet-Higgins, Philos. Trans. R. Soc. London, Ser. A **262**(1132), 511–601 (1968). Copyright 1968 The Royal Society (U.K.).] Only the first ten modes are shown (the lowest curve in the left panel has $k = 1$ and the highest one has $k = 10$). The curves approach their asymptotic forms at each end of the range in L_d (see the text for details). Note the different scales of both the abscissas and the ordinates in the two panels.

progressively more complex. At these early times, there is little sign of an underlying steady balanced flow.

The flow remains unsteady with no significant change in $v_{\rm rms}$ (in a running average) until the end of the simulation at $t = 250$. Over this time, the total energy $\mathcal{H}$ defined in (13) remains conserved to within 0.8%, while the kinetic and potential components vary by 92.7% of $\mathcal{H}$ (in such a way as to nearly conserve total energy). Some of this energy loss is due to the formation of under-resolved small-scale gravity waves by nonlinearity. No explicit numerical damping or de-aliasing is included, but evidently the interpolation used for h results in weak damping under these circumstances (a smaller time step makes no difference).

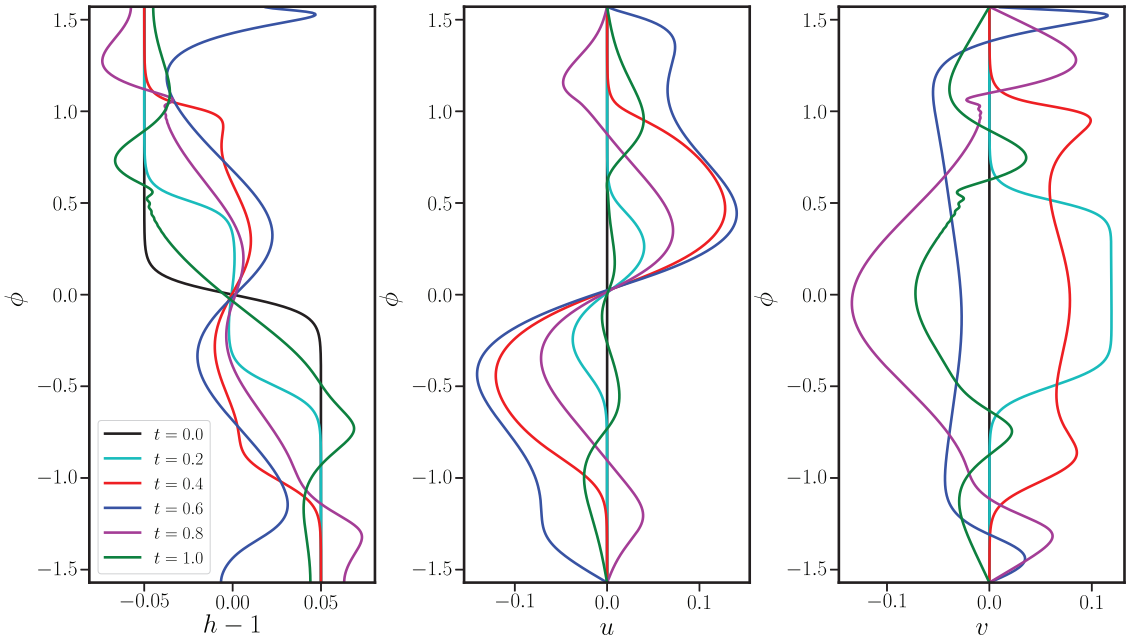

FIG. 2. Early time evolution of a dam-break initial condition for $A = 0.05$, $w = 0.1$ and $L_d = 0.2$. The three panels show $h - 1$, u and v (left to right) at selected times as indicated. Note ϕ is plotted on the ordinate. Numerically, $n = 500$ intervals were used, with a time step $\Delta t = 0.1\Delta a/c = 1/(40nL_d) = 1/4000$.

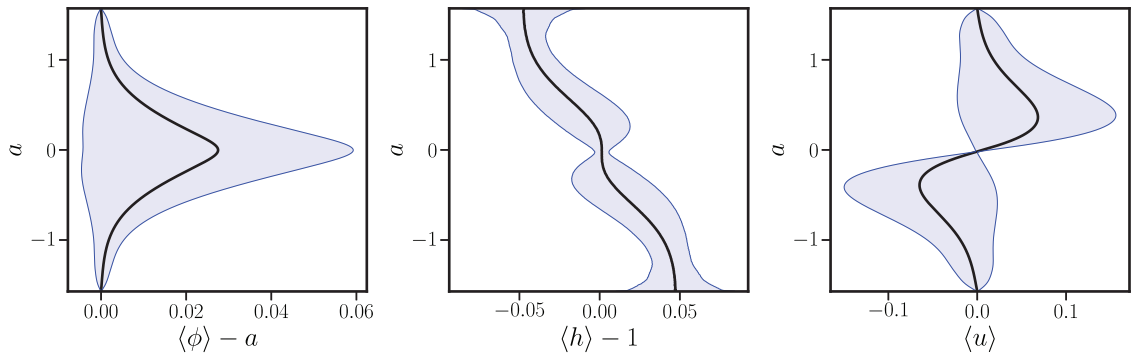

FIG. 3. Time-averaged profiles (over $50 \le t \le 250$, solid black curves) of displacement $\delta = \phi - a$, height anomaly $h - 1$ and zonal velocity u (left to right) for the case examined in Fig. 2 (A = 0.05, $w = 0.1$, and $L_d = 0.2$). The shaded areas show the variability, with the bounding curves indicating ± 1 standard deviations. The Lagrangian coordinate a is plotted on the ordinate.

Figure 3 shows the results of time-averaging the latitudinal displacement $\delta(a, t) \equiv \phi(a, t) - a$, the height anomaly $h(a, t) - 1$, and the zonal velocity $u(a, t)$ vs a, in the same simulation depicted in Fig. 2 at early times. The solid curves show the time-averaged profiles and the shaded regions show the variation (± 1 standard deviation) about the average. First of all, this variation is large, indicating that the inertia–gravity waves play a major if not dominant role in the dynamics. The flow is never close to balanced. Notably, the time-averaged height distribution $\langle h \rangle$ is flat at the equator, where initially it had its steepest gradients. The corresponding zonal velocity distribution $\langle u \rangle$ has a broad eastward jet in the northern hemisphere, and a broad westward jet in the southern hemisphere. The jets appear antisymmetric, but there is a slight asymmetry (see below).

We next compare the time-averaged profiles with the steady balanced flow obtained by solving the nonlinear boundary value problem (16) for $\phi(a)$, using the same distributions $U(a)$ and $M(a)$ as in the simulation above. The balanced height and zonal velocity distributions are diagnosed from $\phi(a)$ using (17). Figure 4 shows the results. The agreement is excellent, with only a slight mismatch of the height distribution near the equator (this discrepancy is likely due to the finite resolution used and the finite period of time averaging). Remarkably, the energy $\mathcal{H}$ of the balanced flow (0.006 001) is just 42.2% of the total (initial) energy (0.014 212) in the dam-break simulation, confirming that the inertia–gravity waves dominate energetically, as already suggested by the large variability in Fig. 3.

To verify that the unsteady motions are purely inertia–gravity waves, the frequency power spectrum of $v(a, t)$ was computed for each a over the period $0 < t \le 250$, then averaged over a (after weighting the spectrum by $\cos a$) to form $\mathcal{P}_v(\omega)$, where ω is the frequency. Figure 5 shows $\mathcal{P}_v$ over an intermediate range of frequencies after log–log scaling. The prominent peaks starting around $\log_{10}\omega = 0.764$ (or $\omega = 5.813$) coincide almost exactly with the frequencies ω_k obtained from the linear analysis (18) for $L_d = 0.2$. This is despite the fact that the linear analysis assumes a basic state of rest—it would be more accurate to use the underlying balanced flow. The magenta dashed lines mark the frequencies of the odd modes ω_1, ω_3, etc., while the green lines mark those for the even modes. For the odd modes, the height anomaly $\hat{h}$ of the eigenmode is also odd in a, i.e., antisymmetric in latitude, while for the even modes $\hat{h}$ is even, see Fig. 6. Moreover, the kth mode exhibits k zeros in the eigenmode $h - 1$ as a function of a.

The most prominent frequency in Fig. 5 corresponds to ω_1 and a mode with one zero in $h - 1$, just like the initial condition $h(a, 0) - 1$ in (19). The next most prominent frequency is ω_3, also an odd mode. In fact all odd modes dominate in $\mathcal{P}_v$; the leading even mode $k = 2$ has less power than any of the odd modes shown. The presence of

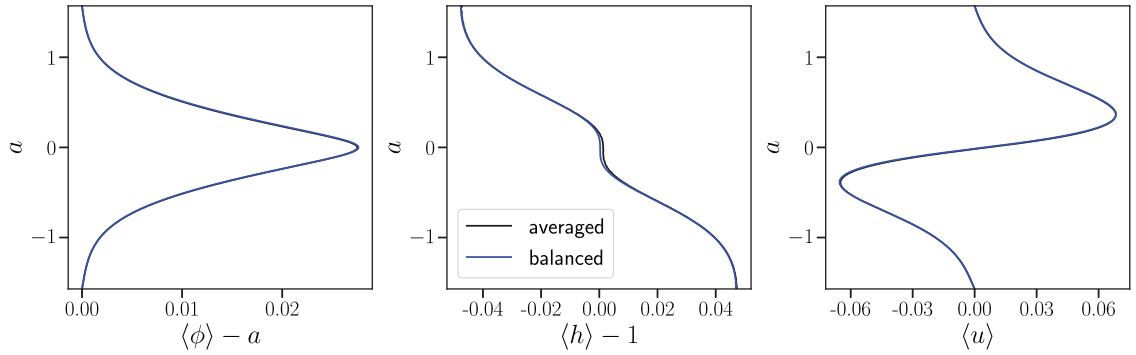

FIG. 4. Comparison of the time-averaged profiles of displacement $\delta = \phi - a$, height anomaly $h - 1$ and zonal velocity u (left to right) with the corresponding steady balanced profiles, for $A = 0.05$, $w = 0.1$, and $L_d = 0.2$. The Lagrangian coordinate a is plotted on the ordinate.

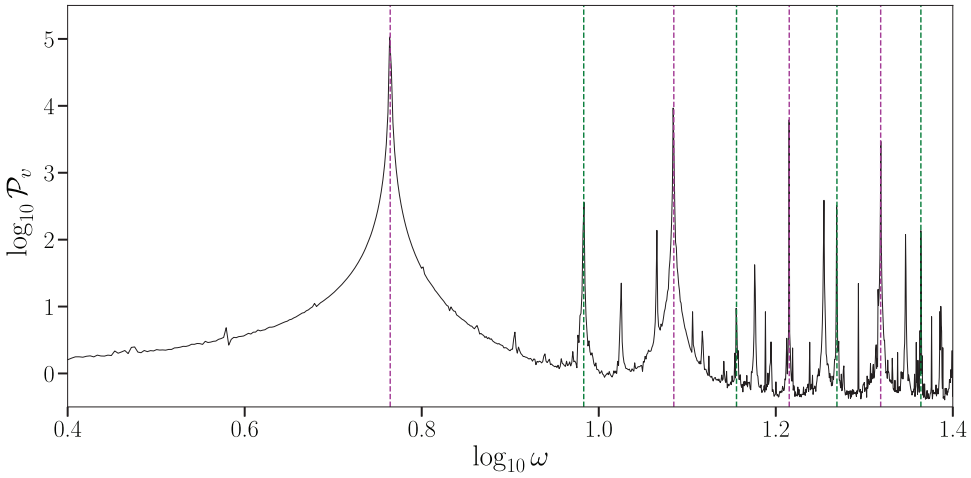

FIG. 5. Frequency power spectrum of the meridional velocity component $v(a, t)$ averaged over a (with area weight $\cos a$) for the simulation examined at early times in Fig. 2. Here, the spectrum was accumulated over $0 < t \leq 250$ using 10^6 time samples. The vertical dashed lines indicate the frequencies ω_k of linear waves on a basic state of rest, with the odd modes in magenta and the even modes in green. Note, $\mathcal{P}_v$ continues to decay toward lower frequencies ω, and also generally diminishes (with weaker peaks) toward higher frequencies.

even modes is partly due to the fact that the underlying balanced flow (the proper basic state) has a height anomaly that is not precisely antisymmetric in a, but it is also partly due to nonlinear wave–wave interactions. Those nonlinear interactions also give rise to additional peaks (sums and differences of two or more frequencies) seen between the marked frequencies. A weaker dam break [reducing A by 10 in (19)] removes nearly all of the secondary peaks and weakens those corresponding to the even modes (not shown).

In summary, a dam break evolves into a set of weakly interacting inertia–gravity waves riding on top of a steady balanced flow. The wave–wave interactions excite new waves at smaller scales, and this is expected to continue indefinitely, leading to a weak forward cascade of wave energy at small scales. This process eventually leads to numerical dissipation of energy, but viscosity would ultimately halt the energy cascade. This evolution has been seen across parameter space (varying A, w, and L_d), so long as A is not too large. When A exceeds 0.2 approximately, energy becomes poorly conserved and a strong forward wave cascade is seen, with many grid-scale variations. This may be an indication of shock formation, and indeed the local Froude number $|v|/(c\sqrt{h})$ can exceed unity. Shocks however violate the long-wave hydrostatic assumption underpinning the shallow-water model. A more accurate model capturing wave dispersion at small scales, such as the nonhydrostatic Green–Naghdi model, is required to go further.[29,30] The lack of dispersion at small scales in the shallow-water model is responsible for shock formation.[31] We hope to report on the dispersive model extension in future work.

IV. BALANCE: EXPLORATION OF PARAMETER SPACE

We next explore the diverse forms of the balanced flows having the same distributions of mass $M(a)$ and angular momentum $U(a)$ as the dam-break initial condition (19). Here, we take the width of the step $w = 0.01$, much smaller than in the example presented in the previous section, to better approximate a step discontinuity in $h(a, 0)$. Recall $M(a) = z - Aw\log(\cosh(z/w))$ and $U(a) = \Omega r^2$, where $r = \cos a$ and $z = \sin a$. For fixed w, the dimensionless balanced flow h and u/Ω depends only on the amplitude A of the step and the Rossby deformation length L_d (the latter is already dimensionless since we have taken the radius of the planet to be 1).

Figure 7 shows balanced flow profiles of a number of quantities for $L_d = 0.2$, and for a range of A. The top row shows displacement $\delta(a) = \phi(a) - a$, height $h(a)$ and scaled zonal velocity $u(a)/\Omega$ plotted against the Lagrangian coordinate a, while the bottom row shows the scaled relative vorticity $\sqrt{1-A}\,\zeta/(2\Omega)$, $h(a)$ and $u(a)/\Omega$ plotted against actual latitude $\phi(a)$. The sharp change in slope of the

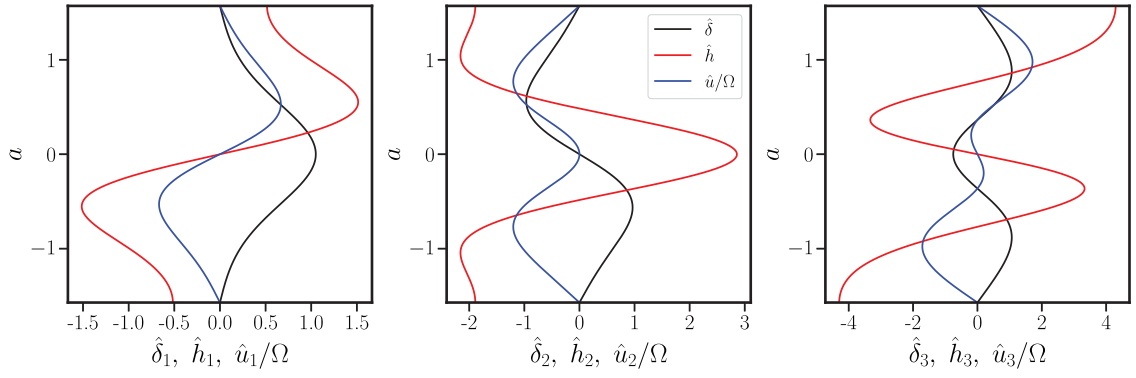

FIG. 6. First three eigenmodes, displayed for the displacement $\hat{\delta}$, height anomaly $\hat{h} = -r^{-1}(r\hat{\delta})'$, and scaled zonal velocity $\hat{u}/\Omega = 2z\hat{\delta}$, for a state of rest and for $L_d = 0.2$. The Lagrangian label, a, is plotted on the ordinate.

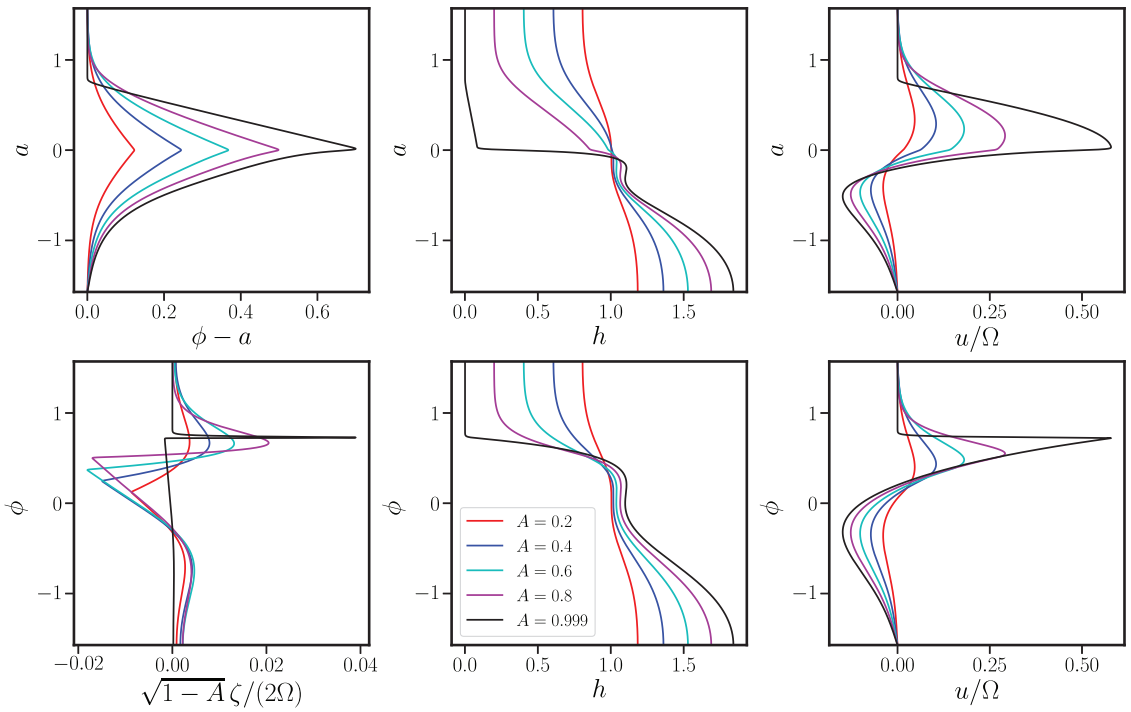

FIG. 7. Summary of the balanced flows for $L_d = 0.2$ and for various values of the amplitude A as indicated. The Lagrangian label a is plotted on the ordinate in the top row, while the latitude ϕ is plotted on the ordinate in the bottom row.

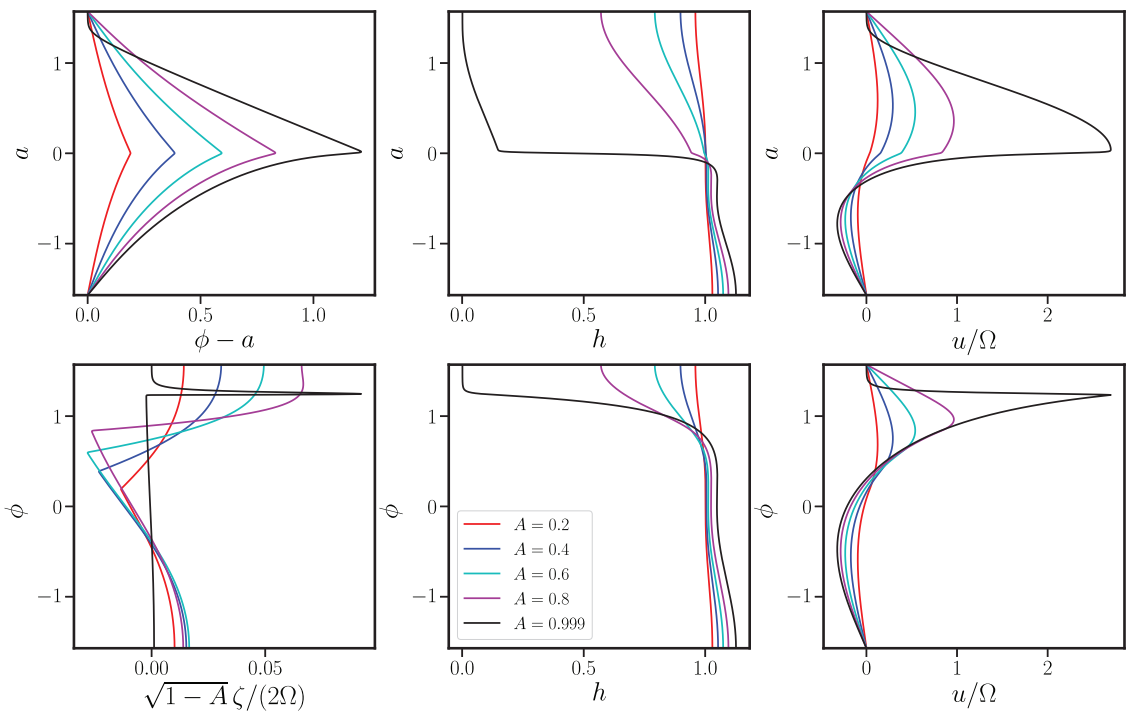

FIG. 8. Summary of the balanced flows for $L_d = 1$ and for various values of the amplitude A as indicated, in the same format as Fig. 7.

displacement $\delta(a) = \phi(a) - a$ is associated with the small step width w. This causes kinks in u and in ζ, but not in $h(a)$ when plotted as a function of actual latitude $\phi(a)$. All flow profiles become increasingly asymmetric as A increases. For $A = 0.999$, we see the most extreme situation in which h appears to vanish at some intermediate latitude in the northern hemisphere. In fact, h is very small but nonzero above this latitude. Only when $A = 1$ exactly does the flow "outcrop": then there is no fluid north of the outcrop line (the limit $A \to 1$ is difficult to analyze; no results are presented here). As shown below, the proportion of energy in the balanced flow (as a fraction of that in the initial state) depends only weakly on A across the entire range of A. The relative vorticity ζ appears to diverge in the limit $A \to 1$ while u abruptly falls to zero at the outcrop line (consistent with divergent ζ). While this outcropping case is mathematically interesting, the local Froude number $\max |u|/\left(c\sqrt{h}\right) = 5.2083$ exceeds unity, and it is therefore likely that any disturbance to this steady flow will rapidly form shocks, violating the long-wave assumption underpinning the shallow-water model used here.[30]

We next consider both smaller and larger Rossby deformation lengths L_d. Recall that L_d controls the "elasticity" of the free surface: when L_d is large displacements in h tend to become small and broad scale; they also propagate fast ($c = 2\Omega L_d$). The opposite is true for small L_d. Figure 8 shows balanced flow profiles for $L_d = 1$, five times larger than considered in Fig. 7. As expected, the profiles extend over a broader latitude range. They are also less asymmetric for smaller amplitudes A. The near outcropping latitude moves poleward (at larger L_d outcropping does not occur), zonal speeds increase (exceeding the maximum rotational speed of the planet Ω for $A > 0.75$ approximately), and the relative vorticity becomes larger. Moreover, the height anomaly $h - 1$ shows a strongly nonlinear dependence on A compared to the case with $L_d = 0.2$ in Fig. 7. All profiles migrate north when plotted against actual latitude $\phi(a)$; hemispheric asymmetry grows with L_d.

Considering now smaller L_d, Fig. 9 shows balanced flow profiles for $L_d = 0.04$, five times smaller than considered in Fig. 7. Now the near outcropping latitude moves equatorward and the flow variations are much more confined near the equator. The height anomaly $h - 1$ stays closely anti-symmetric until A is near its limiting value of 1. Zonal velocities are much weaker, but a bias toward a stronger (though narrower) northern hemisphere jet remains. This asymmetry is due to a shorter effective length scale $c\sqrt{h}/(2\Omega) = L_d\sqrt{h}$ in the northern hemisphere where $h < 1$. It is not evident in $u(a)$ vs a, but only in $u(a)$ vs $\phi(a)$ as changes in ϕ correspond to actual distance, whereas changes in a have no such meaning.

We conclude this section on balanced flows with a general summary of how flow properties like energy depend on L_d and A, keeping $w = 0.01$ fixed. For each balanced flow, we calculate the kinetic and potential energies from

$$\mathcal{K} = \frac{1}{2}\int_{-\pi/2}^{\pi/2} \left(u(a,t)^2 + v(a,t)^2\right) M'(a)\, \mathrm{d}a, \tag{20a}$$

$$\mathcal{P} = \frac{1}{2}c^2 \int_{-\pi/2}^{\pi/2} (h(a,t) - 1)) M'(a)\, \mathrm{d}a, \tag{20b}$$

whose sum gives the total energy $\mathcal{H}$, see (13). Moreover, we diagnose the maximum (polar) Rossby number $\mathrm{Ro} \equiv \max |\zeta|/(2\Omega)$ and the maximum Froude number $\mathrm{Fr} \equiv \max |u|/\left(c\sqrt{h}\right)$.

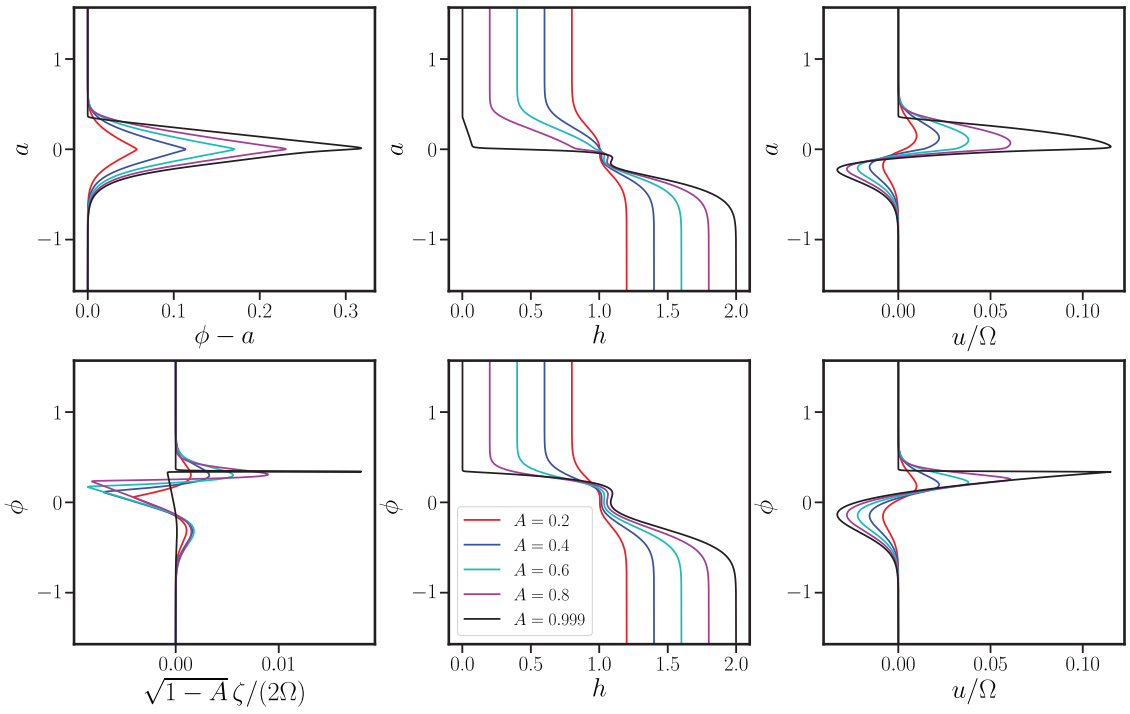

FIG. 9. Summary of the balanced flows for $L_d = 0.04$ and for various values of the amplitude A as indicated, in the same format as Fig. 7.

The results are summarized in Fig. 10. In (a), $\mathcal{H}$ is seen to increase with A as expected, but also with L_d until $L_d = O(1)$. Thereafter, there is little dependence on L_d. This is because the kinetic energy $\mathcal{K}$ dominates $\mathcal{H}$ for $L_d > 1$ [see panel (b)], while the potential energy $\mathcal{P}$ diminishes as the free surface flattens and the flow becomes increasingly "barotropic." The maximum Rossby number Ro also increases with A and L_d, and again shows little dependence on L_d for $L_d > 1$. The kinks in the contours in the middle of this panel are real: they are caused by max $|\zeta|$ occurring for $\zeta > 0$ in one region and for $\zeta < 0$ in another (see lower left panels in Figs. 7–9). The maximum Froude number Fr in panel (d) mainly increases with A but is also larger for small L_d. Above the bold line indicating Fr $= 1$ in this panel, the flow is subject to (spurious) shock formation if disturbed. This only occurs for $A > 0.831$ for small L_d, and not at all for $L_d > 7.3$ when the flow is strongly barotropic.

To better understand the importance of the transient waves in the dam break problem, we consider next the fraction of energy in the balanced flow as a function of L_d and A. First of all, the initial dam break has only potential energy, and the total energy is readily computed from (19) and (13). Elementary integration gives

$$\mathcal{H}_0 = A^2c^2(1 - w\tanh(1/w)).$$

In Fig. 11, we show the balanced state energy $\mathcal{H}$, together with the potential $\mathcal{P}$ and kinetic $\mathcal{K}$ components, divided by $\mathcal{H}_0$. Only three selected values of A are displayed because there is almost no variation with A up to $A = 0.5$ and remarkably little variation overall with A. At small L_d, the balanced flow contains most of the energy of the dam break $\mathcal{H}_0$, and moreover this is mainly potential energy $\mathcal{P}$. Thus, the waves contain only a small proportion of the total energy for small L_d, and this proportion appears to reduce to zero as $L_d \to 0$ (at least when $w < L_d$). For larger L_d, even $O(1)$ values, the situation is reversed: now the balanced flow contains little of the initial energy $\mathcal{H}_0$, and therefore the waves dominate, obscuring any underlying balance.

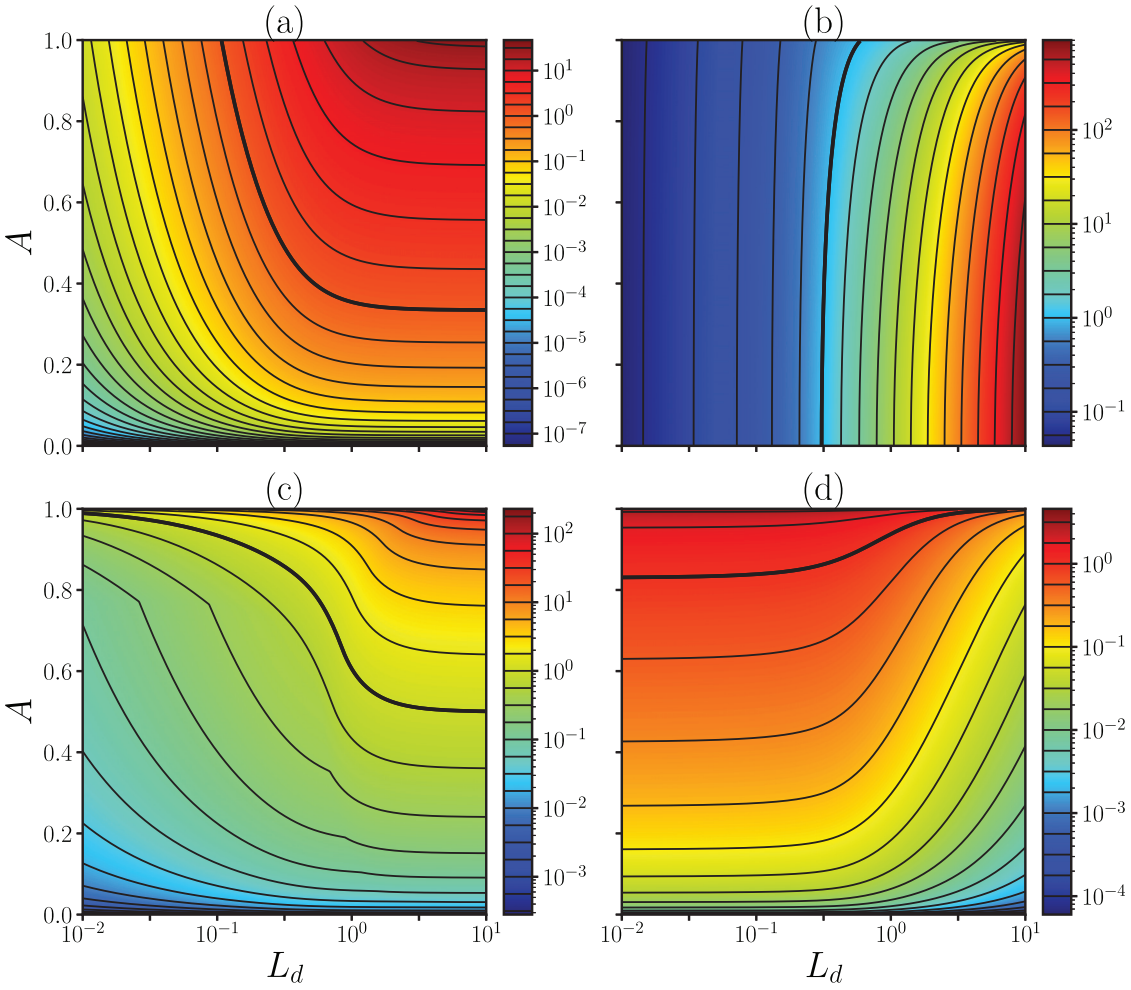

FIG. 10. Various flow properties as a function of the Rossby deformation length L_d and amplitude A. The panels show (a) total energy $\mathcal{H}$, (b) the ratio of kinetic and potential energy $\mathcal{K}/\mathcal{P}$, (c) the Rossby number Ro, and (d) the Froude number Fr. In each panel, the unit level contour is depicted as a bold black curve. The contour spacing is 0.25 in log base 10.

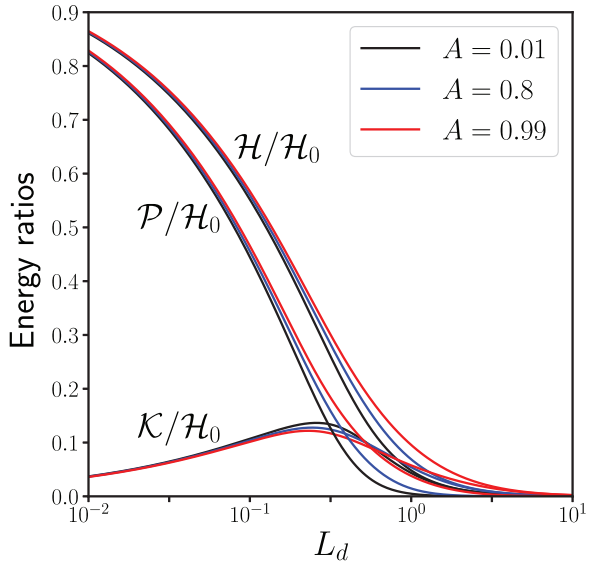

FIG. 11. Fraction of energy in the balanced flow relative to that in the initial dam break (19), as a function of the Rossby deformation length L_d, and for three selected values of the amplitude A. Results are shown for the total, potential and kinetic energy divided by the total energy $\mathcal{H}_0$ of the dam break initial condition (see the text).

Another way of seeing this is to compare the balanced height h in Fig. 8 with the initial condition $h(a,0)$ in (19), which is essentially a step function in a at the small value of w considered. For example, the $A = 0.2$ curve (red) is much flatter than $h(a,0)$; the polar values of balanced h are just 1.0295 and 0.9595, compared to 1.2 and 0.8 for $h(a,0)$. This means that a large proportion of the initial (entirely potential) energy must be released into the waves, and this proportion only increases with L_d. On the other hand, when $L_d \ll 1$ (see, e.g., Fig. 9 for $L_d = 0.04$), the balanced height h remains close to the initial condition except in a small region of $O(L_d)$ width centered on the equator. There is very little difference in potential energy between the balanced state and the initial state, and this difference goes to zero as $L_d \to 0$ (at least when $w < L_d$). This is why so little adjustment takes place when $L_d \ll 1$: the balanced flow is already a close approximation to the initial one.

V. CONCLUSIONS

We have revisited Rossby's famous geostrophic adjustment problem[3,4] first solved in planar geometry under zonal symmetry. Geostrophic adjustment means that any localized initial condition will radiate inertia–gravity waves, all of which eventually escape to infinity, leaving behind a steady, zonal flow in geostrophic balance (a balance between the Coriolis acceleration and the horizontal hydrostatic pressure gradient). Moreover, this zonal flow is uniquely determined by the mass and momentum distributions of the initial fluid particles. These distributions are preserved as the fluid particles displace from the initial to the final, steady adjusted state.

In spherical geometry, the focus of this paper, there is an important difference: the domain is finite. Waves cannot escape, and cannot disappear without some form of damping (which is excluded from the geostrophic adjustment theory and would violate conservation of momentum). As a result, there is no possibility of a final steady flow—indeed conservation of energy forbids it. Any underlying steady flow would have less energy than the initial flow, and the difference, which is entirely due to the presence of inertia–gravity waves, must be conserved. The initial flow already contains these waves; in time they spread through the domain and interact, but never change their energy content.

What then is "adjustment" on a spherical surface, or for that matter, on any finite surface? We argue that any confined flow, at least having zonal symmetry, can be decomposed into a steady "balanced" flow, and a residual unsteady flow consisting entirely of inertia–gravity waves. The balanced flow is the solution to the time-independent equations having the same mass and angular momentum distributions on fluid particles as the initial conditions. In general, this is determined from a highly nonlinear second-order ODE. Results of our time-dependent simulations show that this balanced flow almost exactly corresponds to a long time average of the unsteady flow. We have gone further by comprehensively exploring the wide range of balanced flows permitted, these being determined by the solution of a novel highly nonlinear boundary value problem in a Lagrangian coordinate.

Though nonlinear phenomena such as shocks may develop in the rotating shallow-water equations[32] here the simulated fields after hundreds of days are accurately described by a combination of the balanced steady state and linear waves (the latter cannot leave the bounded domain). A caveat is that our simulations can only access the weakly to moderately nonlinear flow regime in which shocks do not form. The numerical method developed, which exactly enforces conservation of mass and angular momentum on fluid particles, is not appropriate when shocks form. On the other hand, shocks violate the long-wave assumption underpinning the shallow-water model. Arguably, nonhydrostatic dispersive effects should be taken into account at horizontal scales comparable to the fluid depth.[29–31] This is left to future work.

The idealization to zonally symmetric flows in this paper is of course not realistic. Two-dimensional flows also go through a form of adjustment, but the underlying balanced state is neither exact nor steady in general.[25] In such flows, balance is still an important concept, and is often used to explain general features of the large-scale atmospheric and oceanic circulation.[33] In effect, inertia–gravity waves are constantly produced in unsteady flows by spontaneous-adjustment-emission;[34] yet this is countered by adjustment toward an (unsteady) balanced flow. In contrast to the one-dimensional problem studied here in which Rossby waves are filtered out, these waves prevail in a two-dimensional problem. This is left for future work.

ACKNOWLEDGMENTS

The authors report no conflicts of interest.

APPENDIX: HEIGHT INTERPOLATION

Here we provide details of the method to interpolate the height field $h(\phi,t)$ between discrete latitudes $\phi_j(t)$, $j = 0,1,\ldots,n$. Note $\phi_0 = -\pi/2$, while $\phi_n = \pi/2$ are the fixed polar values. In what follows, we suppress the dependence on t.

The numerical method used in Sec. III starts with the fixed mass m_j between latitudes, given by the integral

$$m_j = \int_{\phi_{j-1}}^{\phi_j} h(\phi)\cos\phi\,\mathrm{d}\phi. \tag{A1}$$

The objective is to use the given fixed values of m_j, together with the end point conditions $\mathrm{d}h/\mathrm{d}\phi = 0$ at $\phi = \pm\pi/2$, to determine h as a quadratic spline, see (15), between discrete latitudes. The mass constraints (A1) give

$$m_j = \mu_{0j}h_{j-1} + \mu_{1j}\alpha_{j-1} + \mu_{2j}\beta_{j-1} \quad j = 1, 2, \ldots, n, \tag{A2}$$

where

$$\mu_{k,j} \equiv \int_{\phi_{j-1}}^{\phi_j} p^k \cos\phi\,\mathrm{d}\phi = (\Delta\phi_j)^{-k}\int_{\phi_{j-1}}^{\phi_j} (\phi - \phi_{j-1})^k \cos\phi\,\mathrm{d}\phi, \tag{A3}$$

and $\Delta\phi_j = \phi_j - \phi_{j-1}$. The $\mu_{k,j}$ can be calculated analytically using integration-by-parts, giving

$$\mu_{0,j} = \Delta z_j\,, \quad \mu_{1,j} = z_j + \frac{\Delta r_j}{\Delta\phi_j}\,, \quad \mu_{2,j} = z_j + \frac{2}{\Delta\phi_j}\left(r_j - \frac{\Delta z_j}{\Delta\phi_j}\right), \tag{A4}$$

where $r_j = \cos\phi_j$, $z_j = \sin\phi_j$, $\Delta r_j = r_j - r_{j-1}$, and $\Delta z_j = z_j - z_{j-1}$. The end point conditions $\mathrm{d}h/\mathrm{d}\phi = 0$ at $\phi = \pm\pi/2$ imply $\alpha_0 = 0$ and $\alpha_{n-1} + 2\beta_{n-1} = 0$.

We can re-arrange (A2) to find the unknown h_{j-1} in terms of α_{j-1} and β_{j-1} (also presently unknown)

$$h_{j-1} = w_{0,j} - w_{1,j}\alpha_{j-1} - w_{2,j}\beta_{j-1} \quad j = 1, 2, \ldots, n, \tag{A5}$$

where $w_{0,j} = m_j/\mu_{0,j}$, $w_{1,j} = \mu_{1,j}/\mu_{0,j}$, and $w_{2,j} = \mu_{2,j}/\mu_{0,j}$. The value of h at the north pole is $h_n = h_{n-1} + \alpha_{n-1} + \beta_{n-1}$.

We also enforce continuity of both h and $\mathrm{d}h/\mathrm{d}\phi$ at each interior latitude $\phi = \phi_j$, for $j = 1, 2, \ldots, n-1$. This implies

$$h_{j-1} + \alpha_{j-1} + \beta_{j-1} = h_j, \tag{A6a}$$

$$\alpha_{j-1} + 2\beta_{j-1} = \rho_j\alpha_j, \tag{A6b}$$

where $\rho_j = \Delta\phi_j/\Delta\phi_{j+1}$. Note that the end point condition $\alpha_{n-1} + 2\beta_{n-1} = 0$ is equivalent to setting $\alpha_n = 0$, by (A6b) at $j = n$.

We can eliminate h_{j-1} and h_j in (A6a) using (A5), then apply (A6b) to eliminate β_{j-1} and β_j [using $\beta_j = (\rho_{j+1}\alpha_{j+1} - \alpha_j)/2$] to obtain a tri-diagonal problem for the coefficients α_j

$$\tau_j^-\alpha_{j-1} + \tau_j^0\alpha_j + \tau_j^+\alpha_{j+1} = R_j \quad j = 1, 2, \ldots, n-1, \tag{A7}$$

with

$$\tau_j^- = 2(1 - w_{1,j}) + w_{2,j} - 1, \tag{A8a}$$

$$\tau_j^0 = 2w_{1,j+1} + (1 - w_{2,j})\rho_j - w_{2,j+1}, \tag{A8b}$$

$$\tau_j^+ = w_{2,j+1}\rho_{j+1}, \tag{A8c}$$

$$R_j = 2(w_{0,j+1} - w_{0,j}). \tag{A8d}$$

In (A7), $\alpha_0 = 0$ when $j = 1$, while $\alpha_n = 0$ when $j = n-1$. This simple tri-diagonal problem is easily solved by the Thomas algorithm in $O(n)$ operations.[35,36]

Note that a simpler version of this method can be used to interpolate a function $h(x)$ on a uniform grid in x when only the average value of $h(x)$

$$\bar{h}_j = \frac{1}{\Delta x}\int_{x_{j-1}}^{x_j} h(x)\,\mathrm{d}x,$$

is known, and $\mathrm{d}h/\mathrm{d}x = 0$ at the end points x_0 and x_n. Here, $\Delta x = x_j - x_{j-1}$ is constant, independent of j. There appears to be no simple algorithm available for this in the literature, so it is provided here.

Essentially we can follow the analysis above, simplifying it by replacing the area weight $\cos\phi$ in (A2) by 1, and replacing ϕ by x. Then $\mu_{k,j} = \Delta x/(k+1)$, independent of j; therefore, $w_{k,j} = 1/(k+1)$ for $k > 0$, while $w_{0,j} = \bar{h}_j$. Otherwise (A5)–(A7) still apply. The coefficients in (A8a)–(A8d) greatly simplify: $\tau_j^- = \tau_j^+ = 1/3$, $\tau_j^0 = 4/3$, and $R_j = 2(\bar{h}_{j+1} - \bar{h}_j)$. Hence, we can rewrite the tri-diagonal system in this case as

$$\alpha_{j-1} + 4\alpha_j + \alpha_{j+1} = 6\left(\bar{h}_{j+1} - \bar{h}_j\right) \quad j = 1, 2, \ldots, n-1, \tag{A9}$$

with $\alpha_0 = \alpha_n = 0$. Once the α_j are found, we obtain the other coefficients from $\beta_j = (\alpha_{j+1} - \alpha_j)/2$ and $h_j = \bar{h}_{j+1} - \alpha_j/2 - \beta_j/3$ for $j = 0, 1, \ldots, n-1$. Finally, $h_n = h_{n-1} + \alpha_{n-1} + \beta_{n-1}$.

This method and its generalization above for spherical geometry were both tested using analytical forms for $h(x)$ or $h(\phi)$. The rms error in h was found to scale like n^{-4}, while that for $\mathrm{d}h/\mathrm{d}x$ or $\mathrm{d}h/\mathrm{d}\phi$ was found to scale like n^{-2}.

DATA AVAILABILITY

Data sharing is not applicable to this article as no new data were created or analyzed in this study.

REFERENCES

[1] J. Holton, *An Introduction to Dynamic Meteorology* (Academic Press, 2004), p. 535.
[2] G. Vallis, *Atmospheric and Oceanic Fluid Dynamics* (Cambridge University Press, 2017).
[3] C.-G. Rossby, "On the mutual adjustment of pressure and velocity distributions in certain simple current systems, I," J. Mar. Res. **1**, 15–28 (1937).
[4] C.-G. Rossby, "On the mutual adjustment of pressure and velocity distributions in certain simple current systems, II," J. Mar. Res. **1**, 239–263 (1938).
[5] A. Cahn, "An investigation of the free oscillations of a simple current system," J. Met. **2**, 113–119 (1945).
[6] W. Blumen, "Geostrophic adjustment," Rev. Geophys. Space Phys. **10**, 485–528, https://doi.org/10.1029/RG010i002p00485 (1972).
[7] A. Gill, "Adjustment under gravity in a rotating channel," J. Fluid Mech. **77**, 603–621 (1976).
[8] A. Gill, *Atmosphere-Ocean Dynamics* (Academic Press, 1982).
[9] R. Supekar, V. Heinonen, K. J. Burns, and J. Dunkel, "Linearly forced fluid flow on a rotating sphere," J. Fluid Mech. **892**, A30 (2020).
[10] O. Mickelin, J. Słomka, K. J. Burns, D. Lecoanet, G. M. Vasil, L. M. Faria, and J. Dunkel, "Anomalous chained turbulence in actively driven flows on spheres," Phys. Rev. Lett. **120**, 164503 (2018).
[11] D. Dritschel and M. Ambaum, "A contour-advective semi-Lagrangian algorithm for the simulation of fine-scale conservative fields," Q. J. R. Meteorol. Soc. **123**, 1097–1130 (1997).
[12] D. Dritschel and A. Viúdez, "A balanced approach to modelling rotating stably stratified geophysical flows," J. Fluid Mech. **488**, 123–150 (2003).
[13] A. Mohebalhojeh and D. Dritschel, "Contour-advective semi-Lagrangian algorithms for many-layer primitive equation models," Q. J. R. Meteorol. Soc. **130**, 347–364 (2004).
[14] A. Mohebalhojeh and D. Dritschel, "Assessing the numerical accuracy of complex spherical shallow water flows," Mon. Weather Rev. **135**, 3876–3894 (2007).

[15]D. Dritschel and J. Fontane, "The combined Lagrangian advection method," J. Comput. Phys. **229**, 5408–5417 (2010).
[16]N. Zabusky, M. Hughes, and K. Roberts, "Contour dynamics for the Euler equations in two dimensions," J. Comput. Phys. **30**, 96–106 (1979).
[17]D. Dritschel, "Contour surgery: A topological reconnection scheme for extended integrations using contour dynamics," J. Comput. Phys. **77**, 240–266 (1988).
[18]D. Dritschel, "Contour dynamics and contour surgery: Numerical algorithms for extended, high-resolution modelling of vortex dynamics in two-dimensional, inviscid, incompressible flows," Comput. Phys. Rep. **10**, 77–146 (1989).
[19]Y. Dvorkin and N. Paldor, "Analytical considerations of Lagrangian cross-equatorial flow," J. Atmos. Sci. **56**, 1229–1237 (1999).
[20]N. Paldor and A. Sigalov, "The mechanics of inertial motion on the earth and on a rotating sphere," Physica D **160**, 29–53 (2001).
[21]N. Paldor and A. Sigalov, "Linear waves on the spheroidal Earth," Dyn. Atmos. Oceans **57**, 17–26 (2012).
[22]J. Charney, "On the scale of atmospheric motions," Geofys. Publ. **17**, 3–17 (1948).
[23]T. Warn, O. Bokhove, T. Sheperd, and G. Vallis, "Rossby number expansions, slaving principles, and balance dynamics," Q. J. R. Meteorol. Soc. **121**, 723–739 (1995).
[24]R. Ford, M. McIntyre, and W. Norton, "Balance and the slow quasimanifold: Some explicit results," J. Atmos. Sci. **57**, 1236–1254 (2000).
[25]M. McIntyre and W. Norton, "Potential vorticity inversion on a hemisphere," J. Atmos. Sci. **57**, 1214–1235 (2000).
[26]A. Mohebalhojeh and D. Dritschel, "Hierarchies of balance conditions for the f-plane shallow water equations," J. Atmos. Sci. **58**, 2411–2426 (2001).
[27]M. Longuet-Higgins, "The eigenfunctions of Laplace's tidal equation over a sphere," Philos. Trans. R. Soc. London, Ser. A **262**, 511–607 (1968).
[28]N. Paldor, Y. De-Leon, and O. Shamir, "Planetary(Rossby) waves and inertia-gravity(Poincare) waves in a barotropic ocean over a sphere," J. Fluid Mech. **726**, 123–136 (2013).
[29]A. Green and P. Naghdi, "A derivation of equations for wave propagation in water of variable depth," J. Fluid Mech. **78**, 237–246 (1976).
[30]D. Dritschel and M. Jalali, "The validity of two-dimensional models of a rotating shallow fluid layer," J. Fluid Mech. **900**, A33 (2020).
[31]G. El, R. Grimshaw, and N. Smyth, "Unsteady undular bores in fully nonlinear shallow-water theory," Phys. Fluids **18**, 27104 (2006).
[32]A. Kuo and L. Polvani, "Time-dependent fully nonlinear geostrophic adjustment," J. Phys. Oceanogr. **27**, 1614–1634 (1997).
[33]B. Hoskins, M. McIntyre, and A. Robertson, "On the use and significance of isentropic potential-vorticity maps," Q. J. R. Meteorol. Soc. **111**, 877–946 (2007).
[34]M. McIntyre, "Global effects of gravity waves in the middle atmosphere: A theoretical perspective," Adv. Space Res. **27**, 1723–1736 (2001).
[35]L. Thomas, "Elliptic problems in linear differential equations over a network," Technical Report (Columbia University, New York, 1949).
[36]S. Conte and C. deBoor, *Elementary Numerical Analysis* (McGraw-Hill, New York, 1972).